Available online at www.sciencedirect.com

ScienceDirect

Physics Procedia 66 (2015) 117 – 128

Physics Procedia

C 23rd Conference on Application of Accelerators in Research and Industry, CAARI 2014

Particle Transport along Magnetic Null Lines as Sputter or Antihydrogen Source

R. A. Lane and C. A. Ordonez*

Department of Physics, University of North Texas, Denton, Texas 76203, USA
(Dated: 15 August 2014)

Abstract

Particle transport along null magnetic lines is investigated using classical trajectory Monte Carlo simulations and described as a traveling wave and through diffusion equations. A magnetic null line is defined as a one-dimensional region where the magnetic field magnitude is zero. This region may take any shape in three-dimensional space. The field used in the simulations is generated by two infinite wires of negligible thickness carrying identical current and separated by a small distance. Thus, an infinite magnetic null line exists directly between the wires. The particle trajectories are simulated by solving the equations of motion for each simulated particle of a mono- energetic set. Each is considered individually, with all trajectories starting from the same position along the null line. Each trajectory is simulated until it reaches a specified distance from the initial point or a maximum time elapses. The simulation is repeated using a full set for multiple endpoints and maximum times for ten different amounts of current in the wires. Each current value is selected so that no particles can travel more than seven times the distance between the wires from the null line. The fraction of particles that reach the endpoint in a given time is calculated and used to describe particle transport parallel to the null line. The results are given in normalized, dimensionless units and their possible applications as an antihydrogen source and use in ultra-high purity sputter are discussed. The results are used to find the conditions necessary to obtain a steady and uniform particle flux suitable for ultra-high purity sputter, assuming that plasma is generated near the null line.

Selection and peer-review under responsibility of the Organizing Committee of CAARI 2014

Keywords: magnetic null, antihydrogen, sputter, particle transport

* Corresponding author.
E-mail address: cao@unt.edu

Selection and peer-review under responsibility of the Organizing Committee of CAARI 2014
doi:10.1016/j.phpro.2015.05.017

1. Introduction

The motion of charged particles near a magnetic null curve is investigated using classical trajectory Monte Carlo (CTMC) simulations. A magnetic null curve is a one-dimensional curve in three-dimensional space where the magnetic field is zero along the curve and non-zero elsewhere. Charged particle motion along magnetic null curves is investigated and possible applications are discussed.

The magnetic null curve investigated is formed from the superposition of the magnetic fields of two infinite, straight, parallel wires carrying identical current. A magnetic null line exists directly between the wires. The system is shown schematically in Fig. 1.

The use of magnetic neutral lines in plasma processing has been demonstrated (Uchida 1994; Yoshida and Uchida 1995). Also, charged particle confinement by two magnetic coils that produce a magnetic null curve has been investigated (Lane and Ordonez 2014). The current work investigates how charged particles that are confined by the magnetic system move along magnetic null lines.

CTMC simulations are conducted using the Mathematica (Wolfram Research 2012) code discussed by Lane and Ordonez (2013) and were chosen for their low computational cost and their direct insight into particle motion in the system. The trajectories of monoenergetic particles are solved for, starting at the coordinate origin, and followed until specific conditions are met. Two sets of simulations are conducted. In one, particle transport is investigated by following the trajectories for a set time. Once the time has elapsed, the final axial position, measured parallel to the wires, is recorded. The positions and times are used to calculate the average position and standard deviation of the particles as a function of time. The average velocity and diffusion coefficient are calculated from the average position, standard deviation, and end-times. In a second simulation, the fraction of simulated particles that reach various axial distances from the particle starting point, as measured parallel to the wires, is used to understand the rate at which particles arrive at experimental targets.

Applications of null magnetic curves are discussed. One possibility is enhancing purity in physical vapor deposition (PVD). Another possible application is simultaneous confinement of antiprotons and positrons. Correct conditions in such confinement may lead to antihydrogen production by three-body recombination. Antihydrogen production by three-body recombination has been demonstrated (Amoretti et al. 2002; Andersen et al. 2010; Gabrielse et al. 2012) and proposed experiments will attempt to use antihydrogen to test the fundamental physical properties of antimatter (Kellerbauer 2008; Charman and the ALPHA Collaboration 2013).

The simulations are conducted and the results provided in normalized, dimensionless units. The magnetic fields, their normalization, and the simulation conditions are discussed in Sec. 2. Specifics and results of the investigations into particle motion along null magnetic lines are provided in Sec. 3. The simulations of particles arriving at a specified distance along a null magnetic line, from their starting location are discussed and the results provided in Sec. 4. Statistical uncertainties in the results, applications of magnetic null lines, and areas of future study are discussed in Sec. 5. A short summary of the investigations is provided in Sec. 6.

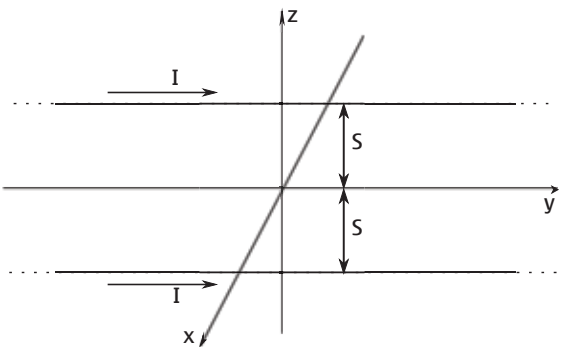

Fig. 1. The system under consideration consists of two infinite, straight, parallel wires carrying current I in the $+y$ direction. The wires are parallel to the y axis and cross the z axis at $z = \pm S$. A null magnetic line exists along the y axis.

2. Classical trajectory Monte Carlo simulations

2.1. System and magnetic field description

The system under consideration consists of two infinite, straight wires that are parallel to the y axis and carry current I in the $+y$ direction. The wires cross the z axis at $z = \pm S$ and are considered to have negligible thickness. The system is shown schematically in Fig. 1. Monoenergetic particles are simulated starting at the coordinate origin, and their trajectories are followed until certain conditions are met. In one set of simulations, the trajectories are followed for a specified time, and their final axial distance in the $\pm y$ direction is calculated. In a second set of simulations, the trajectories are followed until a specified axial distance from the particle starting point in the $\pm y$ direction is reached or a maximum time has elapsed.

The magnetic field is calculated using the superposition principle. The magnetic field of an infinite straight wire everywhere in space in Cartesian coordinates is given by

$$\boldsymbol{B}(x,y,z) = \frac{\mu_0 I}{2\pi}\left(\frac{z\hat{x}}{x^2+z^2} + \frac{-x\hat{z}}{x^2+z^2}\right), \tag{1}$$

where μ_0 is the vacuum magnetic permeability. Thus, for a system consisting of two infinite straight wires located at $z = \pm S$, the magnetic field everywhere in space is

$$\boldsymbol{B}(x,y,z) = \frac{\mu_0 I}{2\pi}\left[\frac{(z+S)\hat{x}-x\hat{z}}{x^2+(z+S)^2} + \frac{(z-S)\hat{x}-x\hat{z}}{x^2+(z-S)^2}\right]. \tag{2}$$

Contour plots of the field magnitude are shown in Fig. 2.

2.2. Normalization conditions and fields

The simulations are conducted within a normalized, dimensionless parameter space. A subscript n is attached to a parameter's symbol to indicate that it has been normalized. The quantities used for normalization are one half the distance between the wires S, particle mass M, magnitude of the particle charge $|q|$, and kinetic energy K. Each of these parameters is normalized such that, $S_n = M_n = |q_n| = K_n = 1$.

Other parameters are normalized by writing them in terms of the un-normalized parameters. A particle's position, velocity, and acceleration are normalized as $\boldsymbol{r}_n = S^{-1}\,\boldsymbol{r}$, $\boldsymbol{v}_n = (MK^{-1})^{1/2}\,\boldsymbol{v}$, and $\boldsymbol{a}_n = (MSK^{-1})\,\boldsymbol{a}$, respectively. The normalized time and magnetic field are written as $t_n = S^{-1}(KM^{-1})^{1/2}\,t$ and $\mathbf{B}_n = |q|S(MK)^{-1/2}\,\mathbf{B}$.

The magnetic field strength is parameterized by the cyclotron radius r_m, of a particle moving in a uniform magnetic field with the same magnitude as the field a distance S from one wire carrying current I. The value of r_m is defined implicitly by

$$\frac{\mu_0 I}{2\pi S} = \sqrt{\frac{2MK}{q^2 r_m^2}}. \tag{3}$$

Equation (3) can be used to find the relation between the normalized magnitude of the magnetic field a distance S_n from a single wire carrying current I_n and the normalized cyclotron radius

$$B_{mn} = \frac{\sqrt{2}}{r_{mn}}, \tag{4}$$

where $r_{mn} = r_m/S$.

The normalization condition for magnetic fields is used to normalize Eq. (2) and is combined with Eq. (3) to give the expression for the total magnetic field everywhere in space,

$$\boldsymbol{B}_n(x_n, y_n, z_n) = \frac{\sqrt{2}}{r_{mn}}\left[\frac{(z_n+1)\hat{x}-x_n\hat{z}}{x_n^2+(z_n+1)^2} + \frac{(z_n-1)\hat{x}-x_n\hat{z}}{x_n^2+(z_n-1)^2}\right]. \quad (5)$$

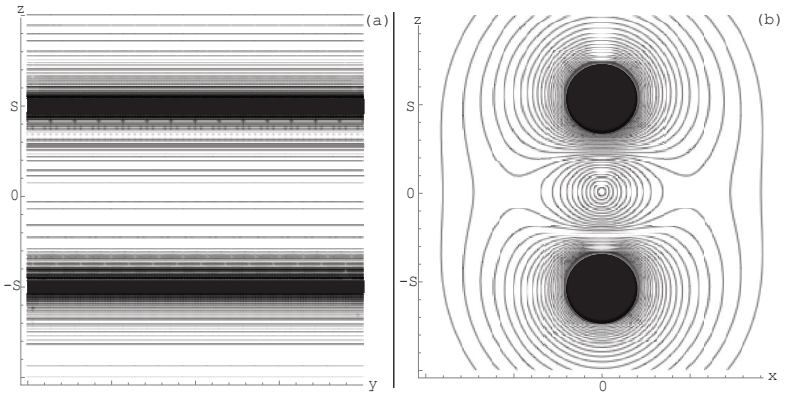

Fig. 2. Contour plots of the magnitude of the magnetic field of the system are shown. The $x = 0$ plane is shown in (a) and the $y = 0$ plane is shown in (b). The contours become infinitesimally close near the wires and appear as solid black.

2.3. Equations of motion

The equations of motion for each particle are obtained from the normalized form of Newton's second law $\boldsymbol{r}''(t_n) = q_n \boldsymbol{r}'(t_n) \times \mathbf{B}_n(\boldsymbol{r}_n)$. Expanding the cross product gives three partial differential equations

$$x_n'' = q_n y_n' B_{n,z}(x_n, y_n, z_n), \quad (6a)$$

$$y_n'' = q_n z_n' B_{n,x}(x_n, y_n, z_n) - q_n x_n' B_{n,z}(x_n, y_n, z_n), \quad (6b)$$

$$z_n'' = -q_n y_n' B_{n,x}(x_n, y_n, z_n), \quad (6c)$$

where x_n, y_n, z_n, and their derivatives are all functions of normalized time. The equations of motion are solved using the initial conditions

$$\boldsymbol{r}_n(0) = \mathbf{0}, \quad (7a)$$

$$\boldsymbol{v}_n(0) = \sqrt{2}\left(sin\theta_0\, cos\,\phi_0\hat{\imath} + sin\theta_0 sin\phi_0\hat{\jmath} + cos\theta_0\hat{k}\right). \quad (7b)$$

Here, ϕ_0 is sampled uniformly on the interval $0 \leqslant \phi_0 < 2\pi$ and θ_0 is sampled on the interval $0 \leqslant \theta_0 \leqslant \pi$ via the sampling expression $\theta_0 = 2\arcsin(\sqrt{R_\theta})$. The sampling expression is obtained by inverting

$$R_\theta = \left(\int_0^{\theta_0} d\theta\, sin\,\theta\right) / \left(\int_0^{\pi} d\theta\, sin\,\theta\right),$$

where R_θ is a random number sampled uniformly on the interval $0 \leqslant R_\theta \leqslant 1$. Through this process, the initial velocity is monoenergetic and equally likely to have any orientation in three dimensional space. The magnitude of the normalized velocity $|\boldsymbol{v}_n| = \sqrt{2}$ is set such that the normalized kinetic energy is $K_n = \frac{1}{2}M_n|\boldsymbol{v}_n|^2 = 1$.

3. Particle motion

3.1. Simulations of particle motion

Simulations are conducted to determine the characteristics of the particle motion. The particle trajectories are calculated starting from the coordinate origin and are followed for a normalized time $t_{n,\max}$. After $t_{n,\max}$ has elapsed, the simulated particle's final axial distance from the origin in the y direction is recorded. The calculation is repeated for a sample set of 3000 trajectories. The simulation is conducted for 10 values of $t_{n,\max}$ for each of 10 magnetic field strengths.

In the simulation of particle motion, the final axial positions in the y direction $y_{n,\max}$, are averaged and the standard deviation is calculated. The average $y_{n,\text{avg}}$, standard deviation $y_{n,\circ}$, number of particles N, and the end-time $t_{n,\max}$, are used to find the average velocity of the group $v_{n,\text{avg}}$, and the diffusion coefficient D_n. These relations are expressed symbolically as

$$y_{n,avg} = N^{-1} \sum_{i=1}^{N} y_{n,max,i}, \tag{8a}$$

$$y_{n,\sigma} = \sqrt{N^{-1} \sum_{i=1}^{N} \left(y_{n,max,i}^2 - y_{n,avg}^2 \right)}, \tag{8b}$$

$$v_{n,avg} = \frac{y_{n,avg}}{t_{n,max}}, \tag{8c}$$

$$D_n = \frac{y_{n,\sigma}^2}{2 t_{n,max}}. \tag{8d}$$

3.2. Traveling wave description

The $y_{n,\max}$ positions are sorted into 20 bins of equal length between $y_n = 0$ and $y_n = \sqrt{2}\, t_{n,\max}$. The resulting histogram of the data is fit with the probability distribution function (PDF) of a shifted normal distribution multiplied by a scaling factor ϵ,

$$P(y_n) = \frac{\epsilon}{y_{n,\sigma}\sqrt{2\pi}} exp\left(\frac{\left(y_n - y_{n,avg}\right)^2}{2 y_{n,\sigma}^2} \right). \tag{9}$$

The fitting parameter ϵ is used to scale the PDF and takes no physical value. The value of ϵ depends on the number of samples and bins. Setting ϵ =1 and finding the area under the curve between two points in Eq. (9),

$$\int_{y_{n,1}}^{y_{n,2}} dy_n \, P(y_n), \tag{10}$$

gives the fraction of particles that will be between $y_{n,1}$ and $y_{n,2}$ at time $t_n = t_{n,\max}$. Furthermore, if $v_{n,\text{avg}}$ is constant with respect to $t_{n,\max}$ and $y_{n,\circ}$ is a linear function of $t_{n,\max}$, then Eq. (9) may be re-written as a traveling wave

$$P\left(y_n, t_{n,max}\right) = \frac{exp\left(\frac{\left(y_n - v_{n,avg}\, t_{n,max}\right)^2}{2\left(c\, t_{n,max}\right)^2} \right)}{\sqrt{2\pi}\, c\, t_{n,max}}. \tag{11}$$

Here, c is a fitting parameter from the linear fit of standard deviations $y_{n,\sigma} = c\, t_{n,\max}$, and Eq. (8c) has been inverted and substituted for $y_{n,\text{avg}}$. The diffusion coefficient is fit with fitting parameter 'd' as a linear function of $t_{n,\max}$,

$$D_n = d\, t_{n,max}. \tag{12}$$

3.3. Results of simulation of particle motion

The final axial positions in the y direction $y_{n,\max}$, were obtained for 3000 simulated particles for $10 \leqslant t_{n,\max} \leqslant 100$ in increments of 10 normalized time units and $0.75 \leqslant r_{mn} \leqslant 1.875$ in increments of 0.125 normalized dimension units. Values for $y_{n,\text{avg}}$ and $y_{n,\sigma}$ were obtained from the CTMC simulations and were used to obtain corresponding values for $v_{n,\text{avg}}$ and D_n, as described in Sec. 3.1.

The $y_{n,\text{avg}}$ values are shown with fits in Fig. 3(a) and the standard deviation values are shown with fits in Fig. 3(b). In Fig. 3(c), the average velocity $v_{n,\text{avg}}$ is shown with linear fits, the slopes of which are approximately zero for all magnetic field strengths. The diffusion coefficients D_n are shown with linear fits in Fig. 3(d).

Table 1 provides values obtained for fitting parameters. Since the value of $v_{n,\text{avg}}$ is approximately constant across the different values of $t_{n,\max}$ for each magnetic field strength tested, the values of $v_{n,\text{avg}}$ are reported as the mean of the 10 $v_{n,\text{avg}}$ values for each magnetic field strength in the second column of Table 1. Thus, the slope of the fit lines for $y_{n,\text{avg}}$ is the corresponding $v_{n,\text{avg}}$ in Table 1, and the $y_{n,\text{avg}}$ values may be calculated through Eq. (8c). The $y_{n,\sigma}$ values may be calculated using the value of the fitting parameter c, and the diffusion coefficients using the fitting parameter d. The c and d values are given in the third and fourth columns of Table 1, respectively.

Particle velocities were monoenergetic and isotropically oriented at the origin but the $y_{n,\max}$ values observed were overwhelmingly positive. With $t_{n,\max}$=100, the highest fraction of particles observed across all magnetic field strengths with negative $y_{n,\max}$ values was 0.032. The fractions are significantly higher with shorter maximum runtimes. With $t_{n,\max}$=10, the highest fraction of particles observed with negative $y_{n,\max}$ values was 0.11. To further investigate the particle motion, abbreviated simulations were conducted with oppositely charged particles. The negatively charged particles yielded $y_{n,\max}$ values that were overwhelmingly negative by similar margins.

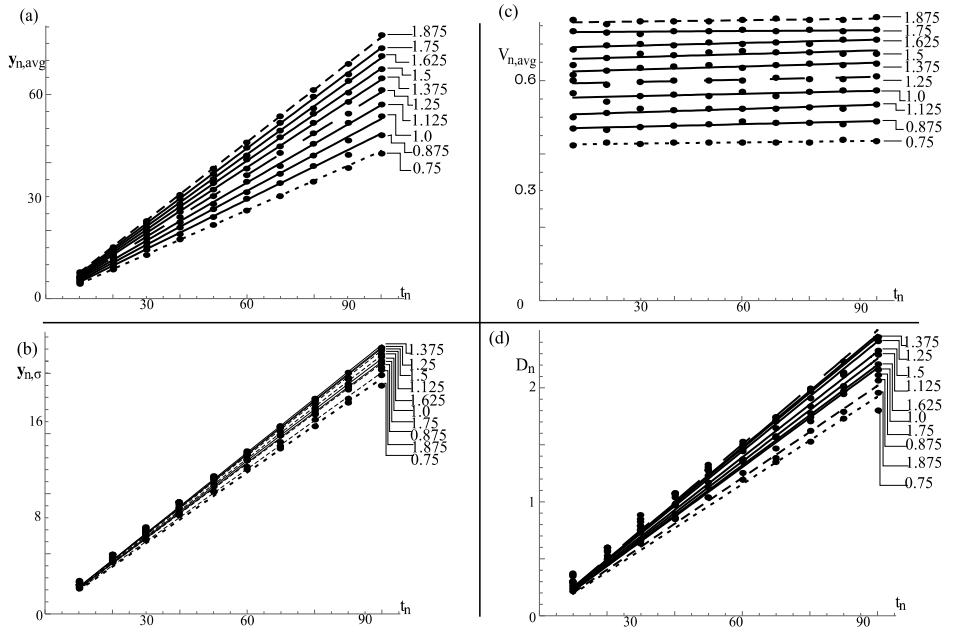

Fig. 3. The average and standard deviations of the final axial positions in the y direction are shown in (a) and (b), respectively. The average velocity and diffusion coefficient are shown in (c) and (d), respectively. The r_{mn} values for each fit line are indicated on the right of each figure.

r_{mn}	$\langle v_{n,\mathrm{avg}} \rangle$	c	d
0.75	0.431	0.196	0.0192
0.875	0.480	0.209	0.0220
1.0	0.521	0.215	0.0232
1.125	0.563	0.221	0.0245
1.25	0.602	0.224	0.0251
1.375	0.637	0.222	0.0247
1.5	0.671	0.219	0.0241
1.625	0.702	0.212	0.0226
1.75	0.735	0.208	0.0217
1.875	0.764	0.201	0.0202

Table 1. Values for fitting parameters for each of the 10 magnetic field strengths considered.

4. Simulated experiment

4.1. Description

In a second simulation, particles that reach a set distance from the coordinate origin are counted. This represents an experiment where Faraday cups are placed at axial distances ±Y from the origin. At time $t_n = 0$, a large number of charged particles are generated within a negligible distance from the coordinate origin and the Faraday cups begin charge integration. The charge is collected and combined into a single integrated value that is normalized by the total charge produced. After a specified time has elapsed, charge integration is stopped and the total charge recorded.

The experiment is repeated for multiple integration times and values of Y. For times shorter than $\mathrm{Y}/|\boldsymbol{v}| = \mathrm{Y}/\sqrt{2}$, no charge should be recorded. At later times, charge should increase with time until the charge recorded is equal to the total charge produced. This experiment is representative of particles incident on a target or a detector.

4.2. Mathematical model

The fraction of particles that reach axial distance Y is modeled using the cumulative distribution function (CDF) of a shifted normal distribution. The mean μ, and standard deviation σ, are used as fitting parameters. The CDF of a normal distribution is

$$CDF(t) = \frac{1}{2} erfc\left(\frac{\mu - t}{\sqrt{2}\sigma}\right), \tag{13}$$

where, erfc(z) is the complimentary error function defined as

$$erfc(z) = \frac{2}{\sqrt{\pi}} \int_z^{\infty} e^{-t^2}\, dt. \tag{14}$$

The simulations return the number of trajectories that reach at least axial distance Y from the origin and the end-time $t_{n,\max}$. Results are normalized by the total number of simulated particles and are fit with Eq. (13) as a function of $t_{n,\max}$. Linear functions are used to extrapolate between the axial distance sampling, i.e.,

$$\mu = aY, \tag{15a}$$

$$\sigma = bY, \tag{15b}$$

where, a and b are fitting parameters.

Equation (13) may be written as a function of time and axial distance by direct substitution of Eqs. (15a) and (15b) yielding

$$F(t_n, Y) = \frac{1}{2} erfc\left(\frac{-t_n + (aY)}{\sqrt{2}(bY)}\right). \quad (16)$$

Here, F(t_n,Y) is the fraction of particles that reach an axial distance Y from the particle starting point in normalized time t_n.

4.3. Conditions for uniform flux

If the particle generation in the simulated experiment occurs at the origin repeatedly, conditions can be set to generate temporally uniform flux at specific axial distances. The conditions include that particle generation occurs with the same number of particles produced in each pulse and is repeated every δt normalized time units. If m pulses occur, then the fraction of the total number of particles that reach an axial distance Y from the origin in a time less than or equal to $t_{n,\max}$ is

$$F_{total} = m^{-1} \sum_{u=0}^{m-1} F(t_{n,max} - u\,\delta t, Y). \quad (17)$$

Here, the normalized time is measured from first production pulse and each production pulse is assumed to have a duration much less than δm.

The rate of simulated particles reaching axial distance Y is considered uniform if over the interval $t_0 \leq t_n \leqslant t_1$, the percent difference between the maximum and minimum values of Eq. (17) is less than a desired value,

$$\frac{max(F_{total})|_{t_0}^{t_1} - min(F_{total})|_{t_0}^{t_1}}{max(F_{total})|_{t_0}^{t_1}} \leq \gamma. \quad (18)$$

The value of γ should be selected to accommodate experimental conditions.

4.4. Results of simulated experiment

Examples and least-squares fits of the fractions of particles reaching axial distance Y and the corresponding end-time $t_{n,\max}$, are shown in Fig. 4. The mean and standard deviation fitting parameters are shown with fits in Fig. 5 (a) and (b). The linear fitting parameters a and b for the mean and standard deviation values are provided in the second and third columns of Table 2.

The minimum $t_{n,\max}$ in which 10, 50, and 90% of the trajectories reach axial distance Y are fit with linear functions of Y

$$t_{n,max} = \alpha Y. \quad (19)$$

The values for 90% and fits are shown for three values of magnetic field strength in Fig. 5(c). The slopes of the fit lines for 10, 50, and 90% for all magnetic field strengths are given in fourth, fifth, and sixth columns of Table 2.

5. Discussion

5.1. Numerical and statistical uncertainty

The change in kinetic energy of the particles throughout the simulation gives an indication of the numerical accuracy of the calculations. It is calculated for a sample simulation of 100 trajectories with Y = 12.5 and the $t_{n,\max}$ where 90% of the trajectories will reach Y. The largest change in kinetic energy observed is 2.6×10^{-6} normalized kinetic energy units.

In the simulated experiment, the sampling intervals and step size over $t_{n,\max}$ are chosen for each parameter pair (r_{mn},Y) to provide at least 20 points between $t_{n,\max} = 0$ and the $t_{n,\max}$ for which 90% of the trajectories reach Y. Additionally, the $t_{n,\max}$ values were selected to evenly cover the interval between $t_{n,\max} = 0$ and twice the minimum $t_{n,\max}$ for which 90% of the particles reach Y. The $t_{n,\max}$ step size is approximately 5% of the $t_{n,\max}$ for which 90% of the particles reach Y.

The fraction of trajectories which reached axial distance Y was found to vary about its mean value with a standard deviation of 9.7 simulated particles per 500. This variation is less than the expected change between $t_{n,\max}$ sampling points. Uncertainty in the $t_{n,\max}$ for which 10, 50, and 90% of the particles reach Y is conservatively estimated at plus or minus one $t_{n,\max}$ step interval.

r_{mn}	a	b	$\alpha_{0.1}$	$\alpha_{0.5}$	$\alpha_{0.9}$
0.75	2.63	0.851	1.474	2.496	4.225
1.875	2.27	0.733	1.431	2.229	3.581
1.0	2.02	0.654	1.287	2.081	3.129
1.125	1.83	0.592	1.270	1.905	2.768
1.25	1.69	0.548	1.152	1.779	2.507
1.375	1.61	0.515	1.132	1.662	2.501
1.5	1.51	0.453	1.094	1.478	2.381
1.625	1.45	0.422	1.080	1.456	2.164
1.75	1.39	0.392	1.081	1.426	1.923
1.875	1.33	0.340	1.000	1.335	1.820

Table 2. The fitting parameters for the mean and standard deviation in the simulated experiment are given in the first two columns. The third, fourth, and fifth columns give the fitting parameter for the linear function of the axial distance Y and the minimum $t_{n,\max}$ for which 10, 50, and 90% of the trajectories reach Y.

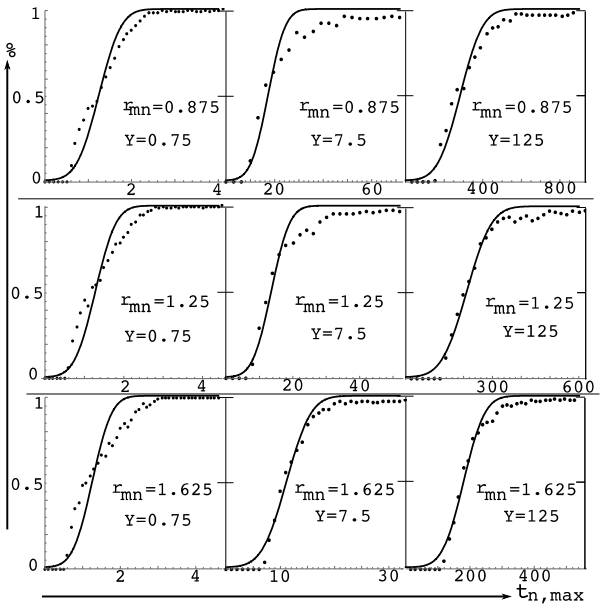

Fig. 4. The fraction of particles which reach axial distance Y from the origin and the corresponding maximum run-time $t_{n,\max}$, are shown with fits for three values of Y for each of three magnetic field strengths.

5.2. Null lines as uniform, high purity sputter source

It may be possible to use null magnetic lines to enhance sputter purity in some physical vapor deposition (PVD) methods. In PVD methods that use non-neutral sputter particles, it may be possible to use null magnetic lines to guide the charged sputter particles from a sputter source to a target. If for a certain distance between the target and the source Y, the parameters are selected to generate uniform flux as described in Sec. 4.3, then the target could be sputtered with a flux that is uniform in time. This sputter may be high purity since charged particles will be guided away from the surrounding walls and other structures.

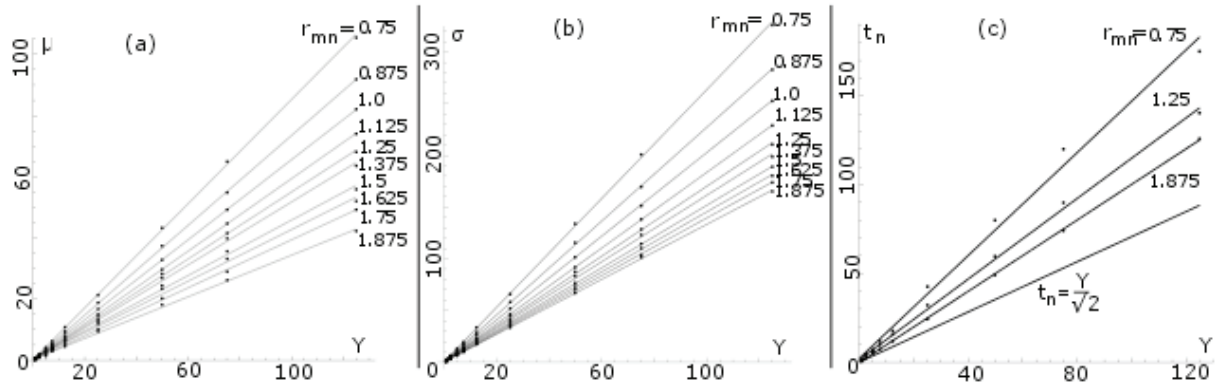

Fig. 5. The mean and standard deviation fitting parameters are shown with linear fits in (a) and (b), respectively. In (c), the $t_{n,\max}$ values for which 90% of the trajectories reach axial distance Y are shown for three values of magnetic field strength with linear fits. The line $t_{n,\max} = Y/s$ for which 90% of the trajectories reach axial distance Y are shown for t.

Null magnetic curves may also have applications in PVD methods that use charged ion bombardment on the sputtering material to generate neutral sputter particles. A null magnetic curve may be able to guide the ions from the ion source to the sputtering material as illustrated in Fig. 6. The neutral sputter particles produced by the ion bombardment on the sputter material would be unaffected by the magnetic field. Alternatively, magnetic null curves could be used to direct charged sputter particles produced during the ion bombardment away from the target. Further theoretical and experimental studies are needed to ascertain the exact characteristics of such a device.

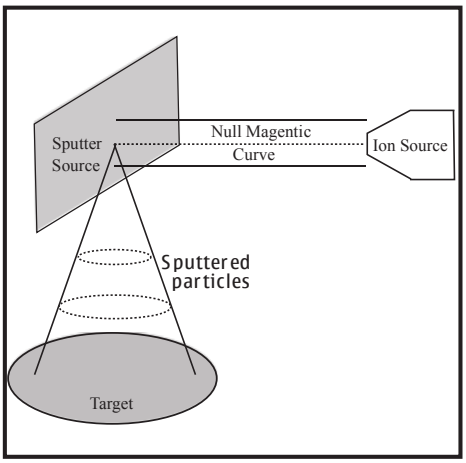

Fig. 6. A possible design for a high-purity physical vapor deposition sputter device.

5.3. Applications to antihydrogen

Multiple experiments are attempting to test the fundamental properties of antimatter (Perez and Sacquin 2012; Widmann 2012; Charmann and the ALPHA Collaboration 2013; Krasnicky 2013). It may be possible to use the null magnetic curves to simultaneously guide antiprotons and positrons with null magnetic curves that may result in antihydrogen production from three-body recombination. As described in Sec. 3.3, the particle drift motion depends on the particle charge. The positrons and antiprotons could be injected at different locations along the null curve and allowed to drift. Conditions can be set to cause the two species to drift through each other, at which point three-body recombination may occur.

The addition of a secondary magnetic field may convert a null magnetic curve to a magnetic minimum. The magnetic minimum produced may be able to transport antihydrogen as well as antiprotons and positrons. Further CTMC studies could test the confinement and guiding properties of a curved magnetic minimum and its capabilities to confine antihydrogen. The magnetic null circle investigated for trapping charged particles by Lane and Ordonez (2014) may be useful in such a device.

6. Summary

Classical trajectory Monte Carlo simulations were conducted to probe the charged particle guiding properties of null magnetic curves. The null magnetic curves considered were generated by two parallel, infinite, straight wires carrying identical current. In one simulation, the trajectories were followed until a maximum time was reached and the final axial position of the simulated particles was investigated. The results are summarized as the average velocity for the particles, fitting parameters for the standard deviation of the final position of the particles, and fitting parameters for the diffusion coefficients.

In a second simulation the simulated particle trajectories were followed until either a maximum normalized time had elapsed or the trajectory reached a specified axial distance from the particle starting point measured parallel to the current-carrying lines. The fraction of particles that reached the specified axial distance from the origin was fit with the cumulative distribution function of a shifted normal distribution as a function of the maximum time. The minimum time necessary for 10, 50, and 90% of the simulated trajectories to reach the specified axial distance was calculated and fit as a function of axial distance. Both sets of fit parameters from this simulation are provided.

In both simulations the trajectories were started at the origin of the coordinate system. All results are normalized and dimensionless and can be applied to specific systems using appropriate conversions. The applications of the results to sputter sources and antiproton experiments are discussed.

Acknowledgments

This material is based upon work supported by the Department of Energy under Grant No. DE-FG02-06ER54883 and by the National Science Foundation under Grant No. PHY- 1202428

References

M. Amoretti *et al*., 2002. “Production and Detection of Cold Antihydrogen Atoms” Nature 419, 456.

G. B. Andresen *et al*., 2010. “Trapped Antihydrogen” Nature 468, 673.

A. E. Charman and the ALPHA Collaboration, 2013. “Description and First Application of a New Technique to Measure the Gravitational Mass of Antihydrogen” Nat. Commun. 4, 1785.

G. Gabrielse *et al*., 2012. “Trapped Antihydrogen in Its Ground State” Phys. Rev. Lett. 108, 113002.

A. Kellerbauer *et al*., 2008. “Proposed Antimatter Gravity Measurement with an Antihydrogen Beam” Nucl. Instrum. Methods B 266, 351.

D. Krasnicky et al., 2013. “AEgIS Experiment Commissioning at CERN” AIP Conf. Proc. 1521, 144.

R. A. Lane and C. A. Ordonez, 2013. “Classical Trajectory Monte Carlo Code for Simulating Ion Beam Focusing or Defocusing with Magnetic Elements Modeled as Current Loops or Current Lines” AIP Conf. Proc. 1525, 97.

R. A. Lane and C. A. Ordonez, 2014. “Classical Trajectory Monte Carlo Simulations of Particle Confinement using Dual Levitated Coils” AIP Adv. 4, 077117

P. Perez and Y. Sacquin, 2012. “The GBAR Experiment: Gravitational Behaviour of Antihydrogen at Rest” Class. Quantum Grav. 29, 184008.

Mathematica, Wolfram Research, Inc., version 9.0.1.0 edition, 2012.

T. Uchida, 1994. “Application of Radio-Frequency Discharged Plasma Produced in Closed Magnetic Neutral Line for Plasma Processing” Jpn. J. Appl. Phys. 33, L43.

E. Widmann, 2012. “Testing CPT S**ymmetry with** A**ntiprotonic** H**elium and** A**ntihydrogen**” AIP Conf. Proc. 1441, 546.

Z. Yoshida and T. Uchida, 1995. “Plasma Production Using Energetic Meandering Electrons” Jpn. J. Appl. Phys. 34, 4213.